Computers & Geosciences 92 (2016) 49–57

Contents lists available at ScienceDirect

Computers & Geosciences

journal homepage: www.elsevier.com/locate/cageo

Research paper

Eliminating the redundant source effects from the cross-correlation reverse-time migration using a modified stabilized division

Qiancheng Liu*, Jianfeng Zhang, Hao Zhang

University of Chinese Academy of Sciences, Beijing, 100049, China

ARTICLE INFO

Article history:
Received 15 March 2015
Received in revised form
12 December 2015
Accepted 2 April 2016
Available online 7 April 2016

Keywords:
Cross-correlation RTM
Source elimination
Stabilized division
High resolution

ABSTRACT

Cross-correlation reverse-time migration is the kernel of two-way wave-equation migration and inversion. However, it more or less tapers the spectrum of receiver data due to a redundant overlay of the source wavelet, whose amplitude spectrum is usually bandlimited and non-flat. To circumvent this issue, there are two optional strategies: whitening the source directly, or preconditioning the seismic traces by division with the amplitude spectrum of the source in the frequency domain. In this paper, we choose the latter one because the source signature is crucial to illumination compensation and seismic inversion. To avoid division by zero, a modified stabilized division algorithm based on the Taylor-expansion is developed. The modified division is easy to complete with computers and can be extend to any order. Moreover, when simulating 2-D source wavefield, the half-integral effect is also considered. We will demonstrate our proposed scheme using the Sigsbee2b synthetic data and a real field data.

1. Introduction

Cross-correlation reverse-time migration (RTM) is widely used in seismic migration and inversion to map seismic traces from data domain to image domain. Two-way wave equation is deployed to accurately describe wavefield propagation even in complex media. RTM (Whitmore, 1983) promises better imaging of steep dips compared to ray-tracing and one-way migration. Also, cross-correlation RTM is closely related to wave-equation velocity and reflectivity inversion, such as full-waveform inversion (FWI) (Laily, 1983; Tarantola, 1984) and least-squares reverse-time migration (LSRTM) (Nemeth et al., 1999; Dai and Schuster, 2013). If all wave-spreading losses are taken in consideration, RTM can be utilized to develop true-amplitude depth migration (Deng and McMechan, 2007).

Several alternative imaging conditions have been proposed for RTM to improve the image to approach the accurate reflection coefficient, though numerically and dimensionless. The ratio of upgoing and downgoing wavefields at temporal and spatial coincidence (Claerbout, 1971), is the original form of physically definition of reflection coefficient (Lumley, 1989). A hybrid method of ray-tracing for the source extrapolation and finite-difference receiver wavefield exploration (Chang and McMechan, 1986), is utilized as the excitation-time imaging condition in prestack RTM. Loewenthal and Hu (1991) use a finite-difference source extrapolation to calculate the excitation-imaging condition according to the arrival time of the maximum-amplitude primary-wave energy. Normalization of the cross-correlated image by source illumination further improves the physical accuracy of the reflectivity information towards true amplitude (Kaelin and Guitton, 2006). The excitation-amplitude imaging condition (Nguyen and McMechan, 2013) divides the propagating receiver wavefield at the imaging time by the maximum source amplitude at each imaging point.

Although the excitation-time (Loewenthal and Hu, 1991) and excitation-amplitude (Nguyen and McMechan, 2013) imaging conditions are cost-effective and partly free of low-wavenumber artifacts, they cannot handle multi-pathing problem well using a single-valued traveltime. Multi-pathing is usually associated with strong lateral velocity variations, which makes more sense for characterizing the reservoir under complicated structures. Cross-correlation imaging condition implicitly includes multi-pathing because all of the propagating energy is preserved through the accumulation process. Source estimation is an important issue in wave-equation migration and inversion (Pratt, 1999; Shin et al., 2007). However, because the amplitude spectrum of the estimated source is usually bandlimited and non-flat, the imaging resolution of RTM will be inherently degraded. Moreover, in wave-equation inversion, the adjoint method (Plessix and Mulder, 2004) indicates that the gradient can be obtained with the cross-correlation between the incident and residual wavefields. The cross-correlation gradients also suffer from this source effect above.

We attempt to design a source-eliminating scheme so that the

* Corresponding author at: University of Chinese Academy of Sciences, Beijing, 100049, China.
E-mail address: liuqc2010@gmail.com (Q. Liu).

http://dx.doi.org/10.1016/j.cageo.2016.04.001
0098-3004/

cross-correlation imaging condition becomes independent of the shape of the source amplitude spectrum. Two strategies are provided: whitening the source directly or preconditioning the receiver traces by division with the source amplitude. We eventually choose the latter one because the first strategy results in an artificial source signature. The estimated source plays important roles in illumination compensation and wave-equation inversion. The source illumination approximates the diagonal of the Hessian (Plessix and Mulder, 2004). In wave-equation inversion, the source wavefield propagating in the forward operator can be used directly to reconstruct the source wavefield in the adjoint operator (Virieux and Operto, 2009). Besides, when propagating source wavefield in 2-D case, it is important to take the half-integral effect into account, because this effect can distort the final imaging waveform.

In the preconditioning step, a division in the frequency domain is performed. To alleviate the introduction of the error caused by a stability factor or the loss of frequency components by the low-cut form (Guitton et al., 2007; Schleicher et al., 2008), we develop a modified stabilized division based on the Taylor-expansion to handle the division-by-zero issue. Specially, our algorithm turns the division issue into a geometrical series which can be easily performed with computers. The order of our Taylor series is flexible, depending on the signal to noise ratio (SNR) of the seismic data. A higher order corresponds to a higher SNR, and vice versa.

The paper is arranged as following: Firstly, we briefly review the conventional cross-correlation imaging condition. Then, we introduce our preconditioner to eliminate the redundant source effects, alternatively, including the half-integral effect in the 2-D source wavefield. Afterward, a modified division algorithm is discussed. Finally, we demonstrate our scheme using the 2D Sigsbee2b synthetic dataset and a real field data.

2. Methods

In this section, we first briefly review the conventional zero-lag cross-correlation imaging condition of RTM; and then propose a preconditioner to enable the imaging condition being independent of the shape of the source amplitude spectrum; alternatively, the half-integral effect implicitly contained in the 2-D wave-equation is discussed. Finally, a modified stabilized division algorithm based on the Taylor-expansion algorithm is used in our preconditioner.

2.1. Conventional cross-correlated RTM imaging condition

The conventional zero-lag cross-correlation RTM imaging condition reads

$$I(\mathbf{x}) = \iint p_S(\mathbf{x}, t; \mathbf{x}_s) p_R(\mathbf{x}, t; \mathbf{x}_s) dt d\mathbf{x}_S, \tag{1}$$

where $p_S(\mathbf{x}, t; \mathbf{x}_s)$ denotes the forward propagation of source wavefield, and $p_R(\mathbf{x}, t; \mathbf{x}_s)$ denotes the backward propagation of receiver wavefield, with the shot at $\mathbf{x}_s$. Eq. (1) is governed by the following system:

$$\begin{cases} \left(\dfrac{1}{v(\mathbf{x})^2}\dfrac{\partial^2}{\partial t^2} - \nabla^2\right) p_R(\mathbf{x}, t; \mathbf{x}_S) = 0, \\ p_R(\mathbf{x}_R, t; \mathbf{x}_S) = D_R(\mathbf{x}_R, t; \mathbf{x}_S), \\ \left(\dfrac{1}{v(\mathbf{x})^2}\dfrac{\partial^2}{\partial t^2} - \nabla^2\right) p_S(\mathbf{x}, t; \mathbf{x}_S) = s(t; \mathbf{x}_S), \end{cases} \tag{2}$$

with $v(\mathbf{x})$ the migration velocity, $s(t; \mathbf{x}_S)$ the source signature at $\mathbf{x}_S$, $D_R(\mathbf{x}_R, t; \mathbf{x}_S)$ the observed receiver data at $\mathbf{x}_R$, and ∇^2 the Laplacian operator. Note that $D_R(\mathbf{x}_R, t; \mathbf{x}_S)$ are imposed as boundary conditions. In our scheme, we assume the knowledge of the source signature.

If the Green's function is defined as

$$\left(\frac{1}{v(\mathbf{x})^2}\frac{\partial^2}{\partial t^2} - \nabla^2\right) G(\mathbf{x}, t - t'; \mathbf{x}_S) = \delta(\mathbf{x} - \mathbf{x}_S)\delta(t - t'). \tag{3}$$

The imaging condition in Eq. (1) can be rewritten as

$$I(\mathbf{x}) = \iiint G_S(\mathbf{x}, \omega; \mathbf{x}_S) W_S(\omega) [G_R(\mathbf{x}, \omega; \mathbf{x}_R) D_R(\mathbf{x}_R, \omega; \mathbf{x}_S)]^* d\omega d\mathbf{x}_R d\mathbf{x}_S, \tag{4}$$

where the superscript * denotes the conjugate transpose, ω is the angular frequency, $W_S(\omega)$ denotes the spectrum of the source, $D_R(\mathbf{x}_R, \omega; \mathbf{x}_S)$ denote the spectra of the receiver data, $G_S(\mathbf{x}, \omega; \mathbf{x}_S)$ and $G_R(\mathbf{x}, \omega; \mathbf{x}_R)$ denote the Green's functions of the source and receiver wavefields, respectively. The backward propagation in the time domain is indicated by the conjugate operator in the frequency domain. The phase of $W_S(\omega)$ can be assumed to be either zero phase or minimum phase, or even mixed phase, depending on the wavelet embedded in the receiver data $D_R(\mathbf{x}_R, \omega; \mathbf{x}_S)$. Because of the conjugate operator *, the cross-correlation imaging condition will produce an image where each reflector is represented as zero-phase bandlimited singular functions with the peak positioned at the reflector. For simplicity, we assume that both the source wavelet and the wavelet embedded in seismic data are rotated to zero-phase.

The estimated source wavelet may behave better than an arbitrary artificial source in RTM and seismic waveform inversion (Pratt, 1999; Shin et al., 2007). In practice, even after being processed carefully, the seismic traces are still slightly mixed-phase. The amplitude spectrum of the estimated source $|W_S(\omega)|$ is usually non-flat and band-limited. In this case, $|W_S(\omega)|$ may act as a filter, tapering the spectra of $D_R(\mathbf{x}_R, \omega; \mathbf{x}_S)$. A deal of valid frequency information is suppressed. The level of suppression depends on the shape of the source amplitude spectrum. Assuming the same signature of the source and receiver wavelets, for example, a Ricker wavelet, the cross correlation of source and receiver wavefields has a cross-reflector width of approximately double the wavelength of each, as shown in Fig. 2c and d, and is a function of incident angle (Tygel et al., 1994). The simplified versions of RTM, such as the excitation-time imaging condition assuming a spike source wavelet (Chang and McMechan, 1986) and excitation-amplitude imaging condition assuming a deconvolution condition (Nguyen and McMechan, 2013), cannot handle the multi-pathing problem well. Even the source-normalized imaging condition (Kaelin and Guitton, 2006), which just corrects for the amplitude scale, has the same resolution as that of the cross-correlated image.

2.2. A preconditioner for source elimination

Now we attempt to eliminate the tapering effect of the bandlimited source from the cross-correlated RTM. There are two options: whitening the source directly or preconditioning the seismic traces by division with the source amplitude spectrum. If we chose the first strategy, regardless of the phase spectrum, the processed source signature approaches some specified wavelets, such as the Ormsby or Klauder wavelet. As a result, the source illumination (Kaelin and Guitton, 2006), which approximates the diagonal of the Hessian (Plessix and Mulder, 2004) to compensate for the wave-spreading loss, is produced by an artificial source. Moreover, because the cross-correlation RTM can be considered as the adjoint operator in wave-equation inversion (Virieux and Operto, 2009), the source wavefield propagated in the Born operator can be directly used to crosscorrelate with the receiver wavefield to produce a gradient. Finally, we choose the second strategy. In this way, the cross-correlation imaging condition can

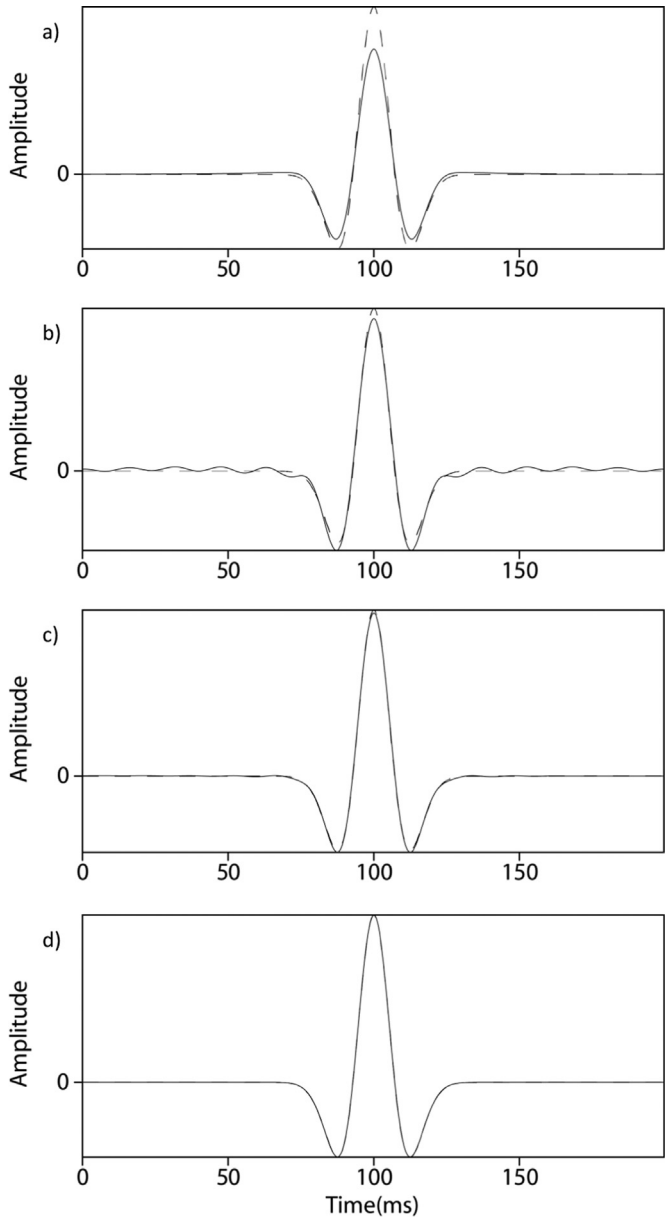

Fig. 1. Comparison of results of $\widehat{W}(\omega) = (W(\omega)/|W(\omega)|)\cdot|W(\omega)|$ using three different stabilized division algorithms. The solid and dash lines indicate the true and the reconstructed wavelets, respectively, in the time domain. Parts (a) and (b) correspond to Eqs. (7) and (8), respectively. Both parts (c) and (d) use our modified stabilized division in Eq. (10), except that $m = 2$ in (c) while $m = 6$ in (d).

be independent of the shape of the source amplitude spectrum.

As long as the source $W_S(\omega)$ is in phase with the embedded wavelet in receiver traces $D_R(\mathbf{x}, \omega; \mathbf{x}_R)$, the cross-correlated imaging condition will produce a singular zero-phase reflector whose peak is centered on the discontinuity of the media. If we prepare the data $D_R(\mathbf{x}, \omega; \mathbf{x}_R)$ with an additional inverse of $|W_S(\omega)|$ as following:

$$I(\mathbf{x}) = \iiint G_S(\mathbf{x}, \omega; \mathbf{x}_S) W_S(\omega) \left[G_R(\mathbf{x}, \omega; \mathbf{x}_R) \frac{D_R(\mathbf{x}_R, \omega; \mathbf{x}_S)}{|W_S(\omega)|} \right]^* d\omega d\mathbf{x}_R d\mathbf{x}_S \tag{5}$$

The amplitude spectra of the reflectors mainly determined by $|D_R(\mathbf{x}_R, \omega; \mathbf{x}_S)|$ are produced where $G_R(\mathbf{x}, \omega; \mathbf{x}_R)$ and $G_S(\mathbf{x}, \omega; \mathbf{x}_S)$ are coincident in time and space.

For numerical implementation, the seismic traces are firstly transformed into the frequency domain, and then prepared as Eq. (5) before wavefield simulation. In 2-D case, by the way, we need to correct for the half-integral filter $(\sqrt{i\omega})^{-1}$ of the source Green's function $G_S(\mathbf{x}, \omega; \mathbf{x}_S)$, as proven by Eq. (A.4) in Appendix A. This is carried out by multiplying $W_S(\omega)$ by $\sqrt{i\omega}$ before the source wavefield propagation. Of note, there is no half-integral effect in the receiver Green's function $G_R(\mathbf{x}, \omega; \mathbf{x}_R)$, which is constructed by imposing receiver traces as boundary conditions. Yet, no such filter exists in 3-D media when handling the wave-equation carefully. Besides, when discretizing the wave-equation with staggered grid, an additional first-order time derivative is added to the mono-source term, resulting in a dipole response of an additional $i\omega$ (Virieux, 1986). Finally, the processed traces are transformed back to time domain and prepared for the backward receiver wavefield propagation. Then, the system governing RTM can be rewritten as

$$\begin{cases} \left(\dfrac{1}{v(\mathbf{x})^2} \dfrac{\partial^2}{\partial t^2} - \nabla^2 \right) \widetilde{p}_R(\mathbf{x}, t; \mathbf{x}_S) = 0, \\ \widetilde{p}_R(\mathbf{x}_R, t; \mathbf{x}_S) = \widetilde{D}_R(\mathbf{x}_R, t; \mathbf{x}_S), \\ \widetilde{D}_R(\mathbf{x}_R, \omega; \mathbf{x}_S) = \dfrac{D_R(\mathbf{x}_R, \omega; \mathbf{x}_S)}{|W_S(\omega)|}, \\ \left(\dfrac{1}{v(\mathbf{x})^2} \dfrac{\partial^2}{\partial t^2} - \nabla^2 \right) p_S(\mathbf{x}, t; \mathbf{x}_S) = s(t; \mathbf{x}_S), \end{cases} \tag{6}$$

where $\widetilde{p}_R(\mathbf{x}, t; \mathbf{x}_S)$ is the receiver wavefield reconstructed by $\widetilde{D}_R(\mathbf{x}_R, \omega; \mathbf{x}_S)$. There is no other changing in the conventional imaging condition Eq. (1) except that $p_R(\mathbf{x}, t; \mathbf{x}_S)$ is replaced with $\widetilde{p}_R(\mathbf{x}, t; \mathbf{x}_S)$. In wave-equation inversion, the source-elimination preconditioner is implemented before residual wavefield propagation per iteration. Since we do not change the frequency bandwidth of $D_R(\mathbf{x}_R, \omega; \mathbf{x}_S)$, no numerical dispersion arises for the receiver wavefield propagation using the original finite-difference stencil.

As we will show by a complexity estimate, the proposed scheme is computationally efficient. In 2-D case, let n_x and n_z be the number of grid points along two axes. The number of receivers is n_r; the number of frequencies of observed data is n_f; the number of discretized time points is n_t. For a common-shot gather, the source-elimination in the third formula of Eq. (6) needs to be done for each frequency of all receiver traces, so we get a total cost of $O(n_r n_f)$; while a wavefield simulation needs a considerable cost of $O(n_x n_z n_t)$. In practice, n_r is less than n_x, n_f is much less than n_t. It concludes that the computational cost of the source-elimination preconditioner is negligible compared to that of the wavefield simulation.

2.3. A modified stabilized division

For the third formula in Eq. (6), when the denominator is retained, some stabilization is required to avoid division by zero. The source-elimination algorithm can be performed by

$$\widetilde{D}_R(\mathbf{x}_R, \omega; \mathbf{x}_S) = \frac{D_R(\mathbf{x}_R, \omega; \mathbf{x}_S)}{|W_S(\omega)| + \epsilon}, \tag{7}$$

where ε is an additive stability factor chosen empirically. In practice, the results of Eq. (7) may be quite sensitive to the stability factor which replaces the small values of $|W_S(\omega)|$. Assuming being sufficiently stable, an improper value of ε may lead to too strong smoothing. To avoid the introduction of amplitude error caused by ε, Schleicher et al. (2008) tests a low-cut form, where stabilization is achieved by zeroing all values of $\widetilde{D}_R(\mathbf{x}_R, \omega; \mathbf{x}_S)$ in case that the denominator $|W_S(\omega)|$ is smaller than ε, i.e.,

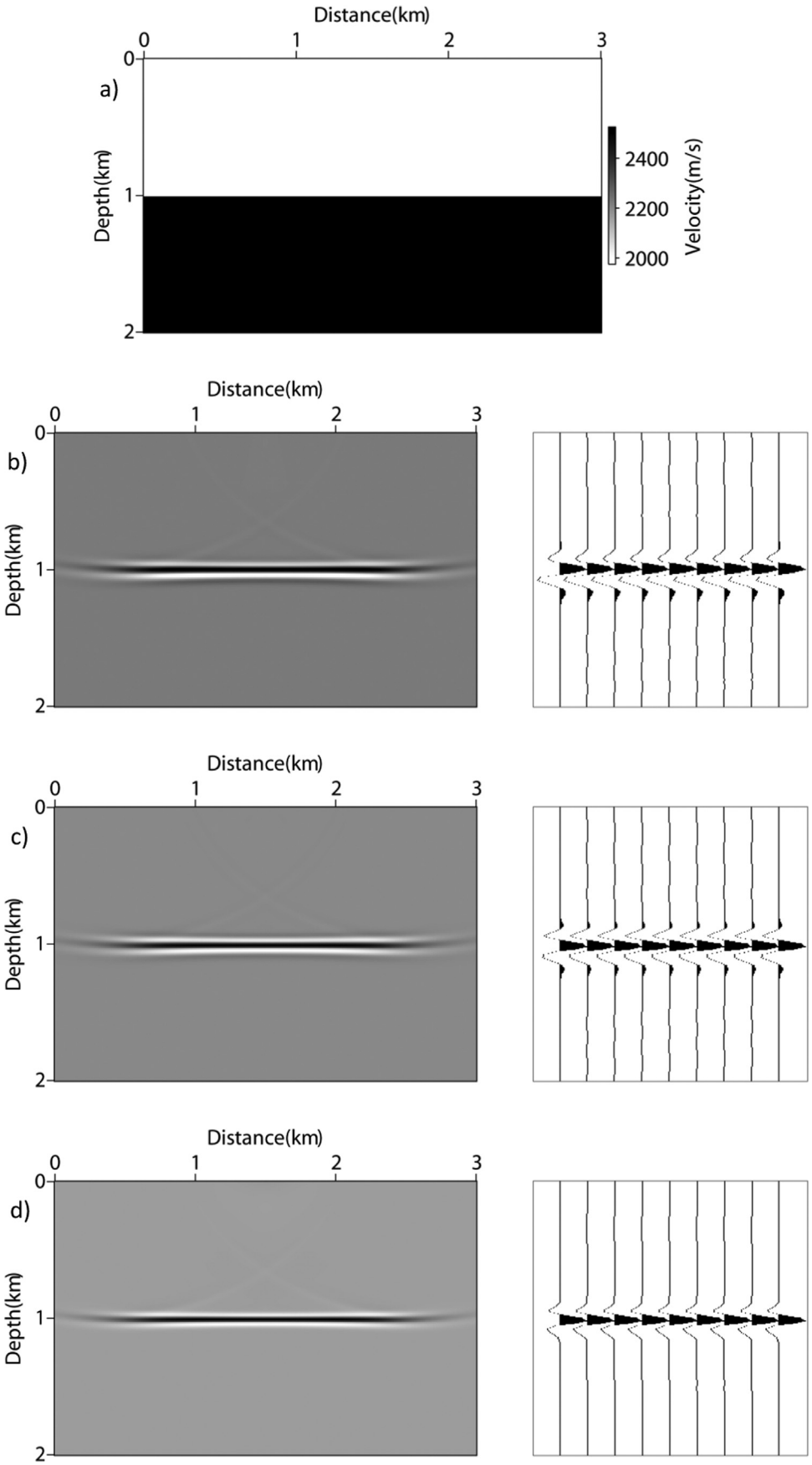

Fig. 2. (a) The two-layer velocity model. A shot is located in the center of the surface. Assuming the synthetic data is rotated to zero phase, the following parts depict, progressively, (b) the original RTM image, (c) the images after half-integral correction, and (d) after source-elimination preconditioning.

$$\widetilde{D_R}(\mathbf{x}_R, \omega; \mathbf{x}_S) = \begin{cases} \dfrac{D_R(\mathbf{x}_R, \omega; \mathbf{x}_S)}{|W_S(\omega)|}, & |W_S(\omega)| > \epsilon \\ 0, & 0 < |W_S(\omega)| \le \epsilon \end{cases}. \tag{8}$$

However, the low-cut form is not recommended because it may suffer from the loss of frequency component. Alternatively, ε could be selected with a technique known as cross-validation, where different ε are selected to deliver very satisfying results. However, robustness and reliability are more important than mathematical accuracy for seismic exploration (Guitton et al., 2007).

In our scheme, based on the Taylor-expansion, we attempt to turn a division problem into a geometrical series. We defined a data-adaptive ε as

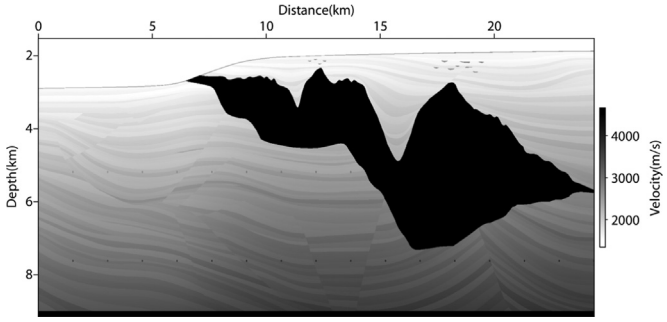

Fig. 3. The 2D Sigsbee2b velocity model.

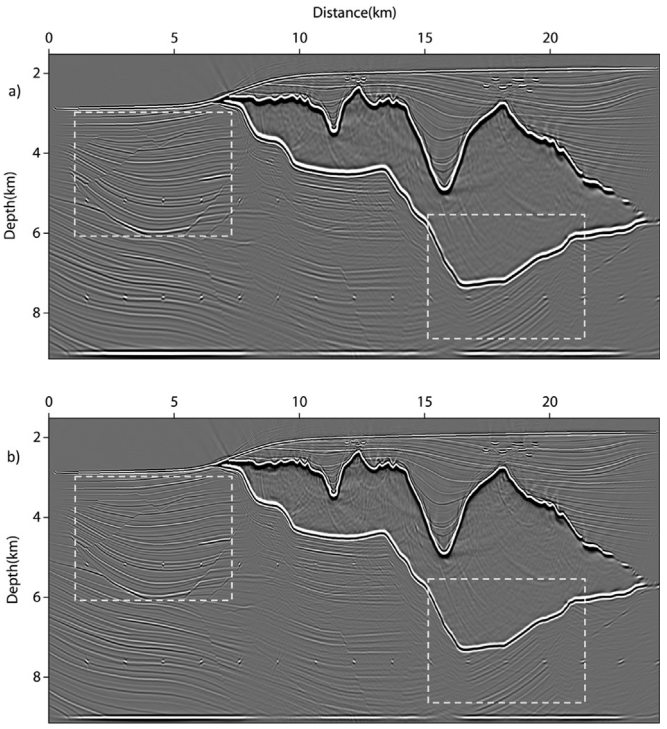

Fig. 5. (a) RTM image without source elimination. (b) RTM image with source elimination. The half-integral effect is considered in both them. No artificial noise is introduced to part (b).

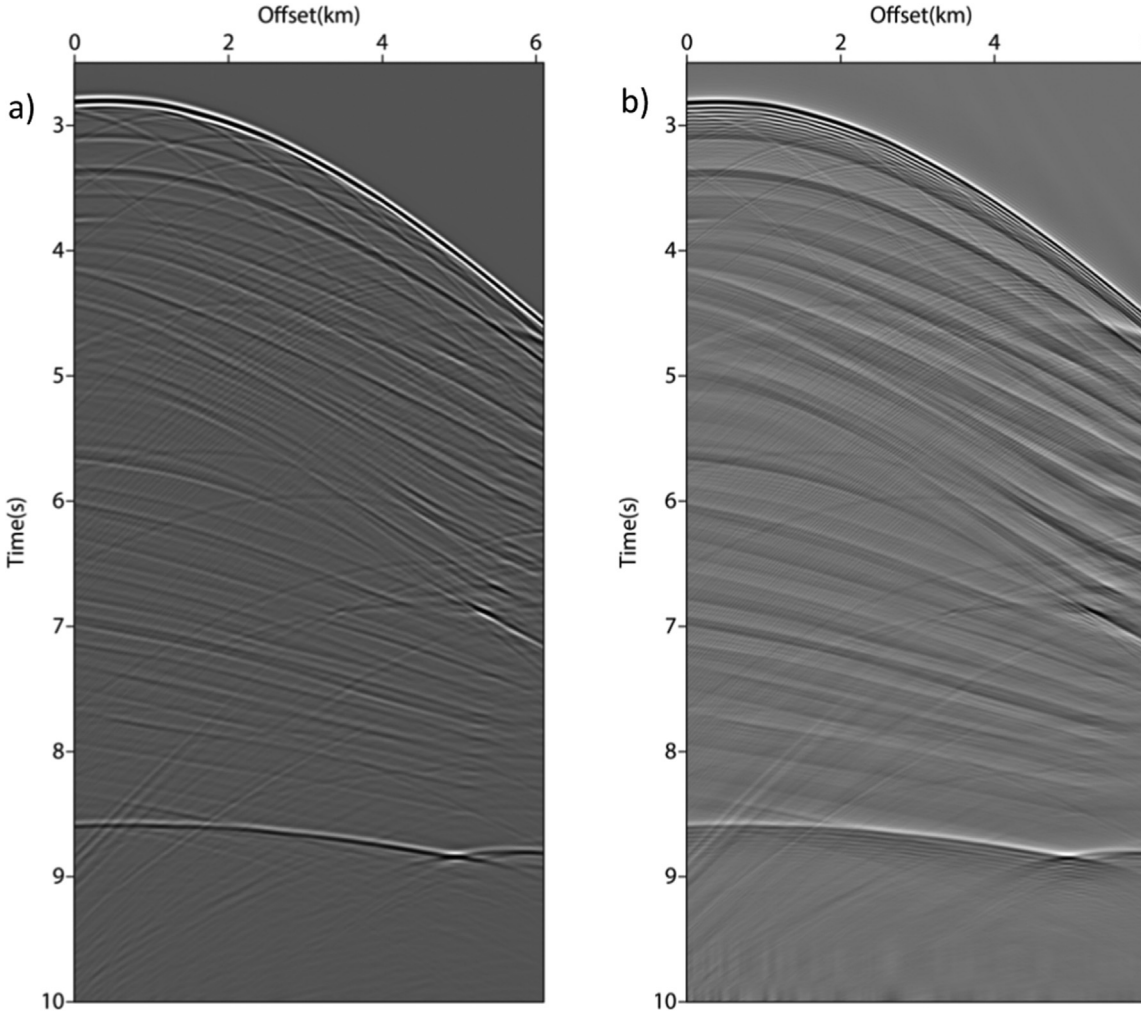

Fig. 4. (a) A common-shot Sigsbee2b synthetic dataset. (b) The traces after source-elimination by Eq. (10).

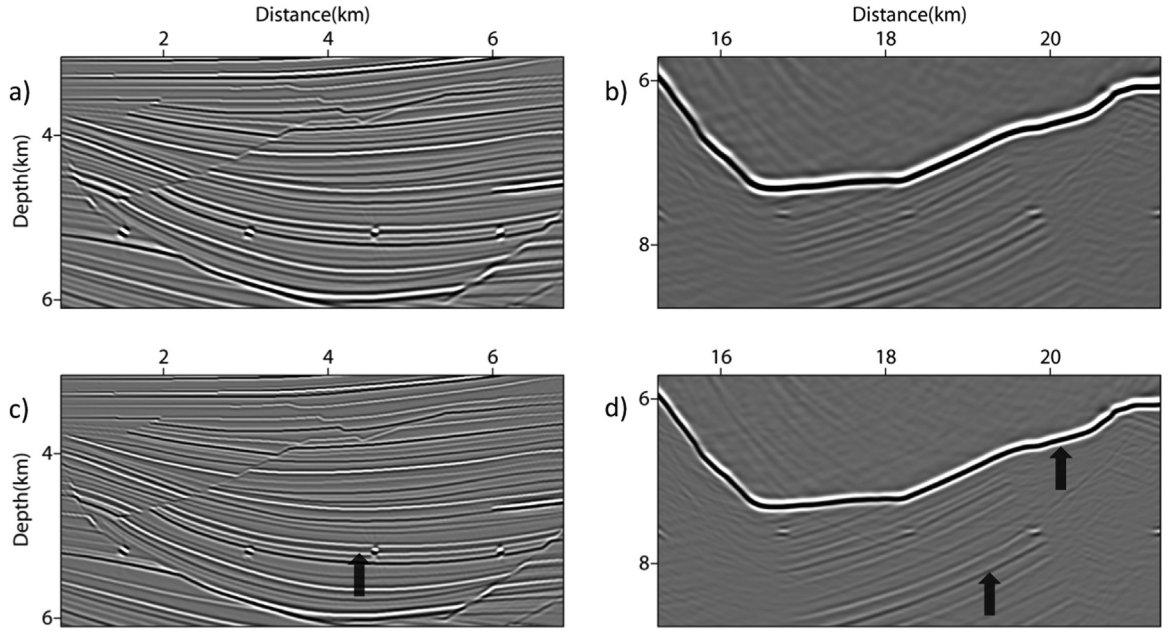

Fig. 6. Zoomed views of the areas enclosed by white boxes in Fig. 5a and b. Compared with (a) and (b), (c) and (d) promise higher resolution, as indicated by the arrows.

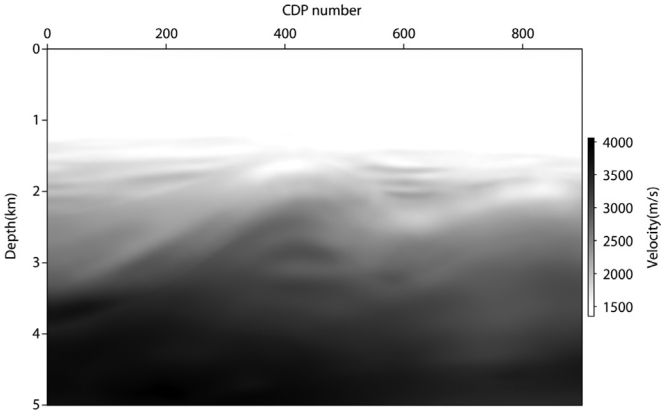

Fig. 7. The migration velocity of a real field data.

$$\varepsilon = \alpha\phi_0 = \alpha\left(\sum_{n\omega}|W_S(\omega)|\right)/n\omega, \tag{9}$$

where ϕ_0 denotes the average value of the source amplitude spectrum $|W_S(\omega)|$, and $0 < \alpha < 1$. As proved in Eq. (B.3) in Appendix B, Eq. (8) can be represented as

$$\widetilde{D_R}(\mathbf{x}_R, \omega; \mathbf{x}_S) = \begin{cases} \dfrac{D_R(\mathbf{x}_R, \omega; \mathbf{x}_S)}{|W_S(\omega)|}, & |W_S(\omega)| > \alpha\phi_0 \\ \dfrac{D_R(\mathbf{x}_R, \omega; \mathbf{x}_S)}{\alpha\phi_0}\sum\limits_{k=0}^{m}\left(1 - \dfrac{|W_S(\omega)|}{\alpha\phi_0}\right)^k, & 0 < |W_S(\omega)| \le \alpha\phi_0 \end{cases}, \tag{10}$$

m denotes the number of terms we collect up to. It is very easy to perform Eq. (10) with computers. For each frequency component, when $0 < |W_S(\omega)| \le \alpha\phi_0$, we need to calculate $1 - |W_S(\omega)|/\alpha\phi_0$ only once. The sum formula is completed with the "for" loops. Of note, we do not recommend taking the sum formula of the series directly, because it may risk again division by zero. Theoretically, for a defined $\alpha\phi_0$, a higher value of m promises a better approximation to the truth-value of the division. In practice, we recommend that a higher value corresponds to a higher SNR, and vice versa. In case of being stable, the division becomes smarter and the output is more reliable compared to Eqs. (7) and (8). Thus, the division-by-zero issue can be partly alleviated. Similar idea is found in Zhang and Zhang (2013).

To verify the behavior of our modified stabilized division, we will test it on a simple division problem as following: $\widehat{W}(\omega) = (W(\omega)/|W(\omega)|)\cdot|W(\omega)|$, where $W(\omega)$ denotes the spectrum of a 20 Hz Ricker wavelet and $|W(\omega)|$ is its amplitude. We first divide $W(\omega)$ by $|W(\omega)|$, and then multiply the quotient with $|W(\omega)|$. The division will be tested using the three stabilized division algorithms above. While being stable, the reconstructed result $\widehat{W}(\omega)$ obtained via a good stabilized division should approach $W(\omega)$ well. For illustration, we set a relative higher value of the stability factor: $\varepsilon = 0.5\phi_0 = 0.5(\sum_{n\omega}|W_S(\omega)|)/n\omega$. Fig. 1 displays a comparison of four results of $\widehat{W}(\omega)$, with the true $W(\omega)$ for reference. All of them are illustrated in the time domain. The first two is obtained using Eqs. (7) and (8), respectively. The last two is obtained using our modified division algorithm in Eq. (10), except that $m = 2$ in Fig. 1c while $m = 6$ in Fig. 1d. The results in Fig. 1c and d indicate that our modified stabilized division behaves better than the former two algorithms. Furthermore, the comparison between Fig. 1c and d demonstrates that in our algorithm, the lower-order terms contribute to the principal value of the division result, and the higher-order terms provide the corrections.

3. Numerical examples

3.1. Two-layer model

A simple 2-D two-layer model is considered for demonstration. The velocity model contains two layers with velocities of 2000 m/s and 2500 m/s, respectively, as shown in Fig. 2a. We generate synthetic data with a single-acquisition geometry where one source is located in the center of the acquisition section and 501 receivers located on the surface of model. A Ricker wavelet with a peak-frequency of 20 Hz is deployed as the source function. The receiver interval is 10 m. The seismic traces are rotated to zero-phase.

The following figures in Fig. 2b–d depict, progressively, the original RTM image, the images after half-integral correction, and after source-elimination preconditioning. As we will see below, in

all figures, reflectors are produced at the corresponding depth. An ideal reflector response should be a zero-phase wavelet. In Fig. 2b, the phase of the reflector is distorted due to the half-integral filter of the 2-D source-wavefield Green's function. After correcting for this filter, in Fig. 2c, a zero-phase wavelet is located where the reflector lies, except the degraded resolution caused by a redundant overlay of the source wavelet. Then, after our source-elimination preconditioning, Fig. 2d shows a zero-phase reflector of the very waveform. No additional artificial noise is introduced.

3.2. Sigsbee2b model

To validate the robustness of our source-eliminating preconditioner, we will performs it on the 2D Sigsbee2b (Paffenholz et al., 2002) synthetic dataset. As shown in Fig. 3, the model contains a sedimentary sequence with a number of normal and thrust faults around the salt body. Due to the strong velocity gradient and the rugose geometry of salt body, the model exhibits the illumination problems and significant multi-paths (Paffenholz et al., 2002). The velocity model composed of 3201 (in X) by 1201 (in Z) points, has an even grid interval 7.62 m (25 ft). The synthetic dataset is generated using the finite-difference stencil with a

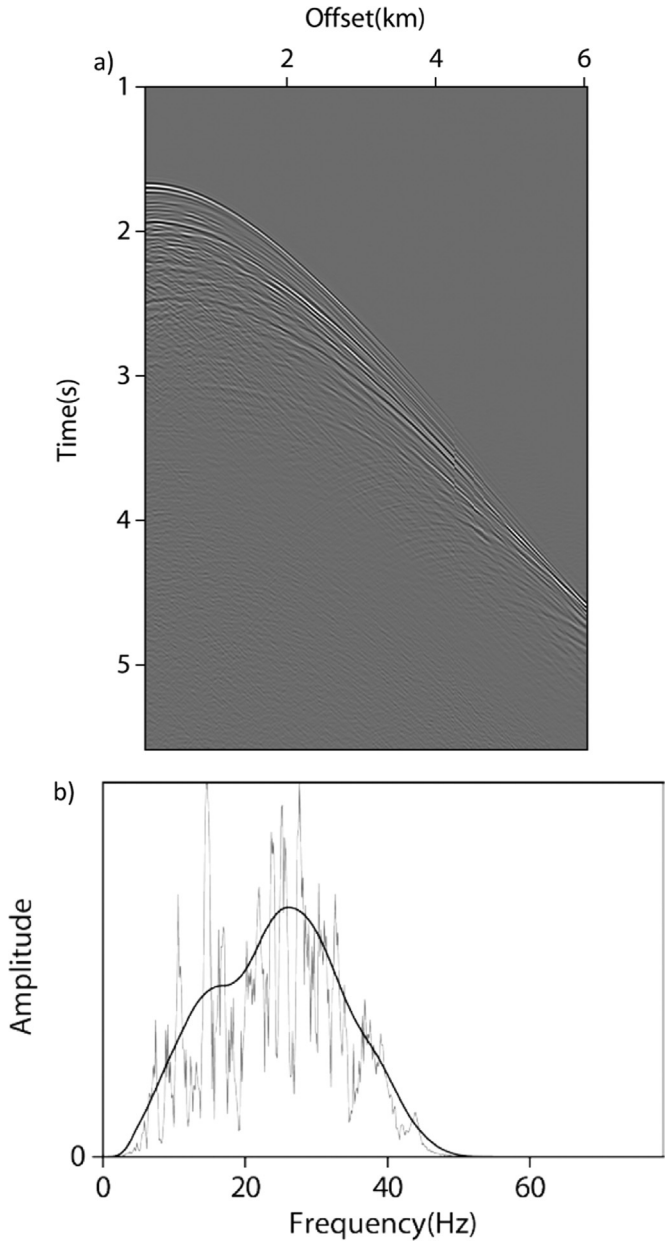

Fig. 8. (a) A common-shot real dataset with shot location 400 CDP number. (b) The black and gray lines represent the amplitude spectra of our estimated source and of the seismic data, respectively.

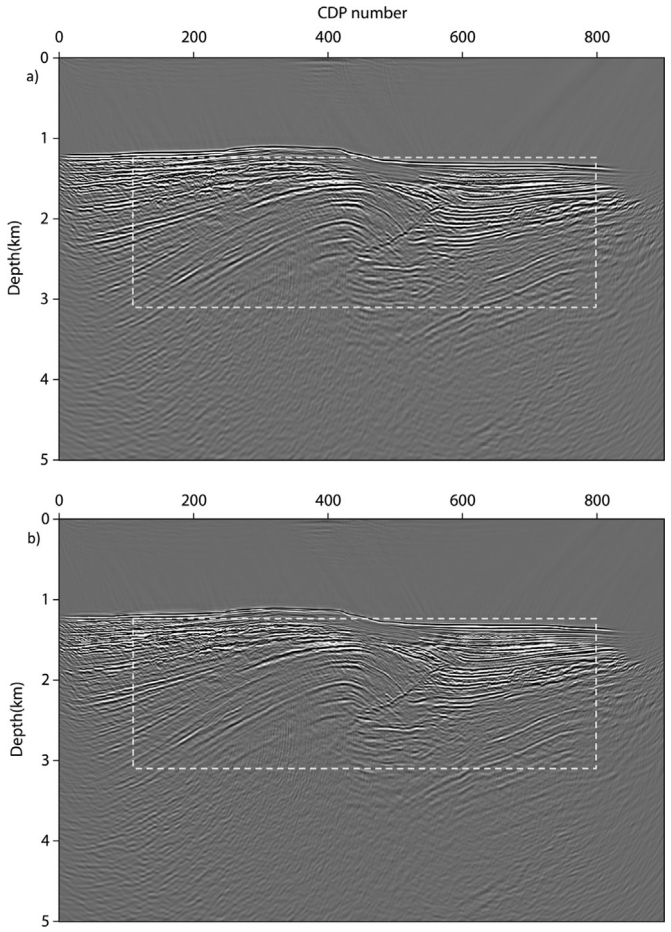

Fig. 9. (a) The conventional RTM image. (b) RTM image with source-elimination preconditioner and half-integral correction. Note that in our scheme, (a) and (b) share the same source illumination.

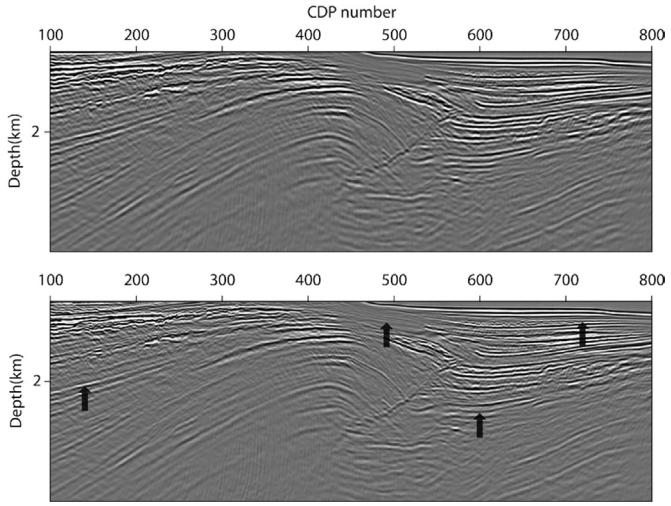

Fig. 10. Zoomed views of the areas enclosed by white boxes in Fig. 9a and b. In part (b), the reflectors are better resolved.

fixed-spread acquisition geometry where 500 shots, distributed from $X=3330$ m (10,925 ft) to $X=26144.2$ m (85,775 ft), are excited with an even interval of 45.72 m (150 ft). 348 receivers are deployed with a 22.86 m (75 ft) interval for each shot to produce the synthetic seismic record. The record length is 12 s with a sample rate 8 ms.

The no-free-surface synthetic dataset with a 20 Hz dominant frequency is used in our RTM. Assuming the knowledge of source signature, we first use Eq. (10) to precondition the seismic traces with $\alpha = 0.05$, $m = 6$. Because the data is clean, no band-pass filter is required. The original data and the processed data using our modified stabilized division are shown in Fig. 4a and b, respectively. Then, we cross-correlate the source-eliminated receiver wavefield with the source wavefield to produce a RTM image. In comparison with Fig. 5a by conventional RTM, our result in Fig. 5b achieves the similar structural image, where the vertical dips and the overhanging salt are clearly imaged, without extra artifacts, and both they are normalized by the same source illumination. However, the comparison of two zoom-view groups in Fig. 6 demonstrates that our scheme helps to promise a higher-resolution image, where seismic events with short wavelength are expected and more subtle reflectors are clear revealed, as indicated by the arrows. It concludes that even with complex media, our source-eliminating preconditioner performs well.

3.3. Real data set

We finally test our scheme on a real marine data set. The data set is acquired by a single cable. The cable has 460 receiver groups at interval 12.5 m. The offset ranges from 100 m to 5750 m. 240 shots at 37.5 m interval are used. Fig. 7 shows the migration velocity. The record length is 8 s with a sample rate 2 ms. Fig. 8a and b shows, respectively, a typical common-shot-gather dataset and the amplitude of an estimated source wavelet obtained using the method in Claerbout (1992).

In this test, we eliminate the source amplitude from the seismic traces using Eq. (10) with $\alpha = 0.08$, $m = 3$. A [2,4,45,50] band-pass filter is followed because the data is somewhat noisy. Also, the half-integral filter embedded in the 2-D Green's function of source wavefield is considered. For comparison, Fig. 9a depicts the conventional RTM image obtained by cross-correlation the source and receiver wavefields directly. Fig. 9b depicts the RTM image obtained by taking the source-elimination preconditioner and the half-integral correction in consideration. The two images share the same source illumination. As shown by the zoomed views in Fig. 10, some features of the image using our schemes are superior to the conventional image. Reflectors appear to be better resolved.

4. Conclusions

Cross-correlation RTM is the kernel of wave-equation migration and inversion. If possible, the imaging reflectors should be independent of the shape of the estimated source amplitude spectrum. We choose to precondition the seismic traces rather than employ an artificial source, since the estimated source is important for illumination compensation and seismic inversion. A modified stabilized division algorithm is used to produce reliable results. Numerical test indicates that our stabilized division performs better than the damping-factor and low-cut forms. Also, the phase rotation is considered when modeling the source wavefield. Numerical examples indicate that our scheme yields shaper seismic events and reveal more subtle details. While eliminate the redundant effects from cross-correlation RTM, other wavefield characteristics related to estimated source are preserved. Furthermore, it is also adaptable to be a useful preconditioner in wave-equation inversion, leading to a cross-correlation gradient of broader spectrum.

Acknowledgments

Thanks to the National Natural Science Foundation of China (under Grant 41574135 and 41330316) for supporting this work. The research was a part of the Elastic Seismic Imaging project sponsored by CNPC. We thank three anonymous reviewers for their constructive comments that improved the manuscript.

Appendix A. Green's functions of forward source wavefield

The 3-D forward propagating Green's function of a point source reads

$$G_{3D}(\mathbf{x}, \mathbf{x}_S, \omega) = \frac{\exp(-i\omega R/c)}{4\pi R}, \tag{A.1}$$

where c denotes the velocity, $\mathbf{x} = (x, y, z)$, $\mathbf{x}_S = (x_S, y_S, z_S)$, $R = \|\mathbf{x} - \mathbf{x}_S\|$. To obtain the 2-D Green's function, we assume a line source parallel to the y-axis instead of a point source. The 2-D Green's function can be derived by integrating the 3-D forward Green's function as following

$$\begin{aligned} G_{2D}(\mathbf{x}, \mathbf{x}_S, \omega) &= \int_{-\infty}^{\infty} G_{3D}(\mathbf{x}, \mathbf{x}_S, \omega) dy_S \\ &= \int_{-\infty}^{\infty} \frac{\exp\left(-i\omega\sqrt{r^2 + Y^2}/c\right)}{4\pi\sqrt{r^2 + Y^2}} dy_S \\ &= -\frac{i}{4} H_0^{(2)}(\omega r/c), \end{aligned} \tag{,(A.2}$$

where $r = \sqrt{(x - x_S)^2 + (z - z_S)^2}$, $Y = y - y_S$, and $H_0^{(2)}(\omega r/c)$ is the Hankel function. We employ the asymptotic formula for the Hankel function at far field, i.e. $r \to \infty$. The asymptotic form of the Green's function Eq. (A.2) is thus given by

$$G_{2D}(\mathbf{x}, \mathbf{x}_S, \omega) = -\frac{i}{4}\sqrt{\frac{2c}{\pi\omega r}} \exp\left(-i\omega\frac{r}{c} + \frac{i\pi}{4}\right). \tag{A.3}$$

Because of $\exp(-i\pi/2) = -i$ and $\exp(i\pi/4) = \sqrt{i}$, we have the final form of Eq. (A.3) as following:

$$G_{2D}(\mathbf{x}, \mathbf{x}_S, \omega) = \sqrt{\frac{1}{i\omega}}\sqrt{\frac{2c}{\pi r}}\frac{\exp(-i\omega r/c)}{4}. \tag{A.4}$$

Its amplitude decays with the inverse square root of the radial distance. In RTM, we can normalize the imaging profile by source illumination to compensate for the amplitude decaying (Kaelin and Guitton, 2006). Note that in 2-D media, the far field expression of the wave equation contains an extra half-integral term $(\sqrt{i\omega})^{-1}$. We should correct for the unexpected 2-D half-integral filter. There is no such filter existing in 3-D media when handling the wave-equation carefully. Besides, when discretizing the wave-equation with staggered grid, an additional first-order time derivative is added to the mono-source term, resulting in a dipole response of an additional $i\omega$ (Virieux, 1986). Those additional effects only exist in the source wavefield, because we usually impose receiver traces as boundary conditions in RTM.

Appendix B. A modified stabilized division base on the Taylor expansion

Firstly, we consider a typical division issue

$$f(x) = \frac{1}{x}, \quad (0 < x < \varepsilon) \tag{B.1}$$

where ε is a given positive fraction. The Taylor series of Eq. (B.1) at $x = \varepsilon$ can be expressed as

$$\begin{aligned} f(x) &= \frac{1}{\varepsilon}\frac{1}{x/\varepsilon} = \frac{1}{\varepsilon}\frac{1}{1-(1-x/\varepsilon)} \\ &= \frac{1}{\varepsilon}\sum_{k=0}^{m}\left(1-\frac{x}{\varepsilon}\right)^k, \quad (0 < x < \varepsilon) \end{aligned} \tag{B.2}$$

where m denotes how many terms we collect up to. This approximation converge to the true function in the region of $|1 - x/\varepsilon| < 1$, including $0 < x < \varepsilon$. Within this region, the higher-degree Taylor polynomial better approximates the truth-value of function $f(x)$.

Following the idea of Eq. (B.2), similarly, in case of $0 < |W_S(\omega)| < \alpha\phi_0$, the sophisticated form of Eq. (10) can be written as

$$\begin{aligned} \widetilde{D_R}(\mathbf{x}_R, \omega; \mathbf{x}_S) &= \frac{D_R(\mathbf{x}_R, \omega; \mathbf{x}_S)}{\alpha\phi_0 \frac{|W_S(\omega)|}{\alpha\phi_0}} \\ &\approx \frac{D_R(\mathbf{x}_R, \omega; \mathbf{x}_S)}{\alpha\phi_0}\sum_{k=0}^{m}\left(1-\frac{|W_S(\omega)|}{\alpha\phi_0}\right)^k, \end{aligned} \tag{B.3}$$

with $\alpha\phi_0 = \alpha(\sum_{n\omega}|W_S(\omega)|)/n\omega$, the adaptive threshold value. $0 < |W_S(\omega)| < \alpha\phi_0$ lies within the convergence region. The Taylor series of higher order are better approximations. In this way, a practical and robust division algorithm is obtained. Since the right-hand-side of Eq. (B.3) is a geometric series, it is very easy to compute the series with computers. Of note, we do not recommend taking the sum formula of the series directly, because it may risk again division by zero.

Appendix C. Supplementary material

Supplementary data associated with this article can be found in the online version at http://dx.doi.org/10.1016/j.cageo.2016.04.001.

References

Chang, W.F., McMechan, G.A., 1986. Reverse-time migration of offset vertical seismic profiling data using the excitation-time imaging condition. Geophysics 51, 67–84.

Claerbout, J.F. (Ed.), 1971. Toward a unified theory of reflector mapping, Geophysics 36, 467–481.

Claerbout, J.F., 1992. Earth Soundings Analysis. Processing Versus Inversion. Blackwell Science.

Dai, W., Schuster, G., 2013. Plane-wave least-squares reverse-time migration. Geophysics 78 (4), S165–S177.

Deng, F., McMechan, G.A., 2007. True-amplitude prestack depth migration. Geophysics 72 (3), S155–S166.

Guitton, A., Valenciano, A., Bevc, D., Claerbout, J., 2007. Smoothing image condition for shot-profile migration. Geophysics 72 (3), S149–S154.

Kaelin, B., Guitton, A., 2006. Imaging condition for reverse time migration. In: 76th Annual International Meeting and Exposition. SEG, Expanded Abstracts, pp. 2594 –2598.

Lailly, P., 1983. The seismic inverse problem as a sequence of before stack migrations. In: Proceedings of Conference on Inverse Scattering. Theory and Application, Society for Industrial and Applied Mathematics. Expanded Abstracts, pp. 206–220.

Loewenthal, D., Hu, L., 1991. Two methods for computing the imaging condition for common-shot prestack migration. Geophysics 56, 378–381.

Lumley, D.E., 1989. Kirchhoff prestack depth migration: imaging conditions and amplitude recovery. In: 59th Annual International Meeting, SEG. Expanded Abstracts, pp. 1336–1339.

Nemeth, T., Wu, C., Schuster, G.T., 1999. Least-squares migration of incomplete reflection data. Geophysics 64, 208–221.

Nguyen, B.D., McMechan, G.A., 2013. Excitation amplitude imaging condition for prestack reverse-time migration. Geophysics 78 (1), S37–S46.

Paffenholz, J., Mclain, B., Zaske, J., Keliher, P.J., 2002. Subsalt multiple attenuation and imaging: observations from the Sigsbee2B synthetic data set. In: 72nd Annual International Meeting, SEG. Expanded Abstract, pp. 2122–2125.

Plessix, R.E., Mulder, W.A., 2004. Frequency-domain finite-difference amplitude-preserving migration. Geophys. J. Int. 157, 975–987.

Pratt, R.G., 1999. Seismic waveform inversion in the frequency domain, Part 1: theory and verification in a physical scale model. Geophysics 64, 888–901. http://dx.doi.org/10.1190/1.1444597.

Schleicher, J., Costa, J.C., Novais, A., 2008. A comparison of imaging conditions for wave-equation shot-profile migration. Geophysics 73 (6), S219–S227.

Shin, C., Pyun, S., Bednar, J.B., 2007. Comparison of waveform inversion. Part 1: Conventional wavefield vs. logarithmic wavefield. Geophys. Prospect. 55, 449–464. http://dx.doi.org/10.1111/j.1365-2478.2007.00617.x.

Tarantola, A., 1984. Inversion of seismic reflection data in the acoustic approximation. Geophysics 49, 1259–1266.

Tygel, M., Schleicher, J., Hubral, P., 1994. Pulse distortion in depth migration. Geophysics 59, 1561–1569.

Virieux, A., Operto, S., 2009. An overview of full-waveform inversion in exploration geophysics. Geophysics 74 (6), WCC1–WCC26.

Virieux, J., 1986. P-SV wave propagation in heterogeneous media, velocity-stress finite difference method. Geophysics 51, 889–901.

Whitmore, N., 1983. Iterative depth migration by backward time propagation. SEG Technical Program Expanded Abstracts 1983, pp. 382–385.

Zhang, J., Zhang, H., 2013. Robust incident-angle field estimation: a one-way wave propagator approach. Explor. Geophys. 44, 245–250.